remote sensing

Article

Location and Activity Changes of Slow-Moving Landslides Due to an Earthquake: Perspective from InSAR Observations

Caihong He [1], Qian Sun [1,2,*], Jun Hu [3] and Rong Gui [3]

[1] College of Geographic Science, Hunan Normal University, Changsha 410081, China
[2] Key Laboratory of Geospatial Big Data Mining and Application, Hunan Normal University, Changsha 410081, China
[3] School of Geosciences and Info-Physics, Central South University, Changsha 410083, China
* Correspondence: sandra@hunnu.edu.cn

Abstract: Strong earthquakes can not only trigger many landslides in a short period of time but can also change the stability of slopes in the earthquake area, causing them to be active for a long time after the earthquake. Research on the variation of slow-motion slopes before and after earthquakes can help us to better understand the mechanism of earthquake-affected landslides, which is also crucial for assessing the long-term landslide risk in seismically active areas. Here, L-band ALOS-2 PALSAR-2 images are utilized with the SBAS-InSAR algorithm to monitor and assess the location and activity changes of slow-moving landslides in the Iburi region (Hokkaido, Japan) before and after an earthquake occurred on 6 September 2018. Unlike previous studies, which focused on single typical landslides, we tracked all the landslides within a 33 × 55 km region close to the epicenter. According to the results, the majority of the co-seismic landslides that quickly failed during the earthquake are now stable, and a few of them are still moving. In contrast, due to near-field seismic shaking, certain slopes that did not show substantial surface changes during the earthquake period continued to move and eventually developed into slow-moving landslides. In addition, it can be seen from the spatial distribution of slow-moving landslides after the earthquake that this distribution is not only dependent on strong earthquake seismic vibration or the hanging-wall effect. Far-field weak vibrations can also accelerate landslides. Additionally, we discovered that the earthquake made the unstable slopes move more quickly but also tended to stabilize the slopes that were already in motion before the earthquake. The various response modes of slow-moving landslides to seismic events are related not only to the intensity of seismic vibration but also to the geological conditions of the region and to the size of the landslide itself. These findings are extremely valuable for studying the mechanism of earthquake-affected landslides.

Keywords: slow-moving landslides; InSAR; earthquake; landslide activity; Iburi

check for updates

Citation: He, C.; Sun, Q.; Hu, J.; Gui, R. Location and Activity Changes of Slow-Moving Landslides Due to an Earthquake: Perspective from InSAR Observations. *Remote Sens.* **2023**, *15*, 1977. https://doi.org/10.3390/rs15081977

Academic Editors: Fabio Rocca and Cristiano Tolomei

Received: 14 January 2023
Revised: 3 April 2023
Accepted: 3 April 2023
Published: 8 April 2023

1. Introduction

Strong earthquakes are followed by changes in mountain landscapes, ranging from small-scale soil cover destruction to large-scale rock collapse. Because earthquake-induced landslides are frequently enormous, widespread, and deadly, they generally result in a substantial number of deaths as well as material and financial damage [1,2]. Unfortunately, strong earthquakes not only change the mountain landscape and cause a large number of seismic landslides but also destabilize the slopes after the earthquake, greatly increasing the risk of geological hazards in the seismic zones [3]. As a necessary consequence, exploring the movement process of landslides within the earthquake zone is an essential part of analyzing landslide inception mechanisms and assessing landslide risk. However, because of a lack of in situ observations, it is currently difficult to evaluate the impacts of earthquakes on landslides' kinematic processes.

Remote sensing images have become an essential data source for investigating earthquake-induced landslides, and remote sensing techniques have become a popular way to circumvent a lack of field data [4,5]. The automated or semi-automatic interpretation of remote sensing images can help us to identify earthquake-induced landslides and to better understand the factors that influence landslides [6]. Most studies focus on co-seismic landslides [7–9], which have distinct landslide morphology on optical images while disregarding slow-moving landslides after earthquakes. However, as mentioned earlier, strong ground vibrations increase the instability of slopes and, thus, the potential for slow-moving landslides to form. Spreading at a pace of millimeters to meters per year down slopes, slow-moving landslides are difficult to locate using morphological features and are vulnerable to external influences such as earthquakes and rainfall [10]. Slow-moving landslides may cause damage to man-made structures on the ground in the future and may affect post-earthquake reconstruction. Therefore, it would be useful to determine the location of slow-moving landslides in the earthquake zone and to analyze their behavior before and after the earthquake to avoid losing human money and property.

The InSAR (interferometric synthetic aperture radar) technique can precisely measure surface deformation in the line-of-sight (LOS) direction and, thus, is frequently used to detect slow-moving landslides. Time-series InSAR approaches, such as PS-InSAR (persistent scatterer InSAR) [11], SBAS-InSAR (small baseline subset InSAR) [12], and SqueeSAR [13], can reduce the impacts of atmospheric and topographic residual noises as well as temporal decoherence; therefore, they can offer significant technological support for the continual monitoring of surface deformations associated with landslides. These approaches have been used to investigate landslides in seismic zones, such as detecting slow-moving landslides after earthquakes [14,15] and tracking the deformation processes of specific significant landslides [16]. Using InSAR technology, Song et al. [17] created a dataset of earthquake-accelerated landslides that occurred in Central Italy's earthquake zone between 2016 and 2017, and they investigated the factors that affected the changes in landslide movement in the seismic area. Similarly, Cai et al. [18] investigated the behavioral changes of slow-moving landslides in the 2017 Jiuzhaigou earthquake zone and summarized the effects of earthquakes on slow-moving landslides into three modes, i.e., acceleration, triggering, and reactivation. However, the patterns of change in the kinematics and spatial location of slow-moving landslides before and after earthquakes, along with the associated factors influencing their changes in kinematics and spatial location, are largely unknown. Further examples of slow-moving landslides in seismically active locations should be investigated, allowing for a more thorough evaluation of landslide risk in the seismic area.

In this context, this investigation focuses on the 2018 Hokkaido–Iburi earthquake in Japan. First, by exploiting 10 scenes of L-band ALOS-2 PALSAR-2 data acquired during 2017–2019, we obtained the locations of slow-moving landslides before and after the earthquake with the SBAS-InSAR algorithm. Then, the different dynamic motion processes of slow-moving landslides before and after the earthquake were compared. Finally, we analyzed the relationships between these processes and seismic events in terms of time and space, and we explored other possible factors. This work not only helps with post-disaster reconstruction in the area but also gives us a new perspective on the perturbation processes of landslide motion caused by earthquakes.

2. Materials and Methods

2.1. Study Area

The research region lies in the southern portion of Hokkaido, Japan, and is characterized by north–south-trending thrust faults caused by the westward migration of the Kuril Arc sliver and its collision with northeastern Japan as a result of the Pacific Plate's oblique sinking since the Miocene (Figure 1) [19]. Figure 2 shows the geological framework of the study area. On 6 September 2018, a magnitude 6.6 earthquake at a depth of 37 km struck the Iburi area in eastern Hokkaido, Japan. The geological bedrock in the region is made up of non-marine sedimentary rocks from the Late Miocene [20]. These sedimentary rocks are covered by 1.5 m-thick layers of volcanic debris, which contribute to the area's soft foundation [21]. At the same time, torrential rains caused by a typhoon two days before the earthquake induced a considerable volume of water into these sediments, resulting in high soil moisture in the area at the time of the earthquake. According to the data supplied by the Geospatial Information Authority of Japan, the earthquake triggered over 6000 landslides, most of which were shallow [22]. The results of the aftershock mechanism inversion indicate the presence of a slow-moving east-dipping reverse fault (a relatively rising fault on the hanging wall along the fault plane [23]) near the epicenter, and a future earthquake of magnitude 7.7 or greater is possible [24].

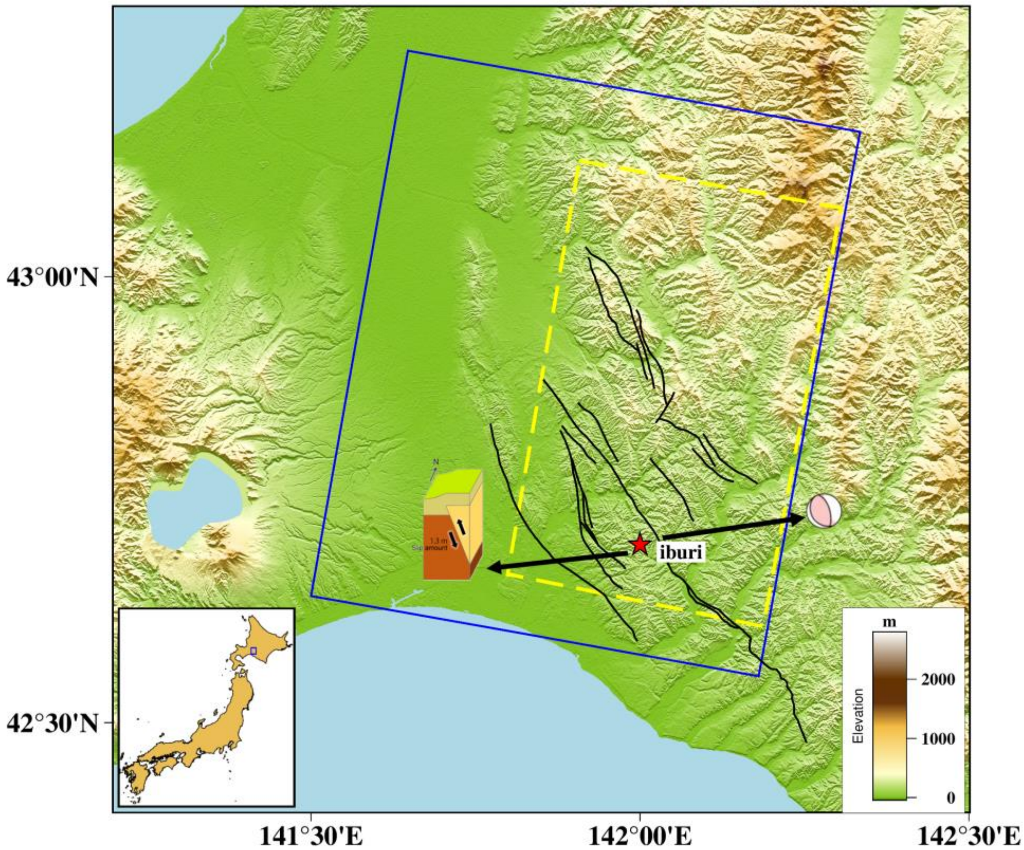

Figure 1. Geographic location of the study area. The blue line represents the coverage of ALOS-2 PALSAR-2 data, and the yellow line represents the scope of this study. The faults, crustal velocity, epicenter, and slip model are from the Geospatial Information Authority of Japan (GSI), while the focal mechanism is from the United States Geological Survey (USGS).

2.2. Materials

Given the dense vegetation cover in the research location, we used L-band ALOS-2 PALSAR-2 data provided by the Japan Aerospace Exploration Agency (JAXA). Table 1 summarizes the key parameters of the used data. We employed HH polarization mode single-look complex (SLC) format data in a strip-map mode for SBAS-InSAR processing in this investigation, involving 10 descending images, and the data were obtained for the whole time period spanning the pre-earthquake, co-earthquake, and post-earthquake periods. To assess the influence of topography during InSAR processing, we employed a digital elevation model (DEM) with a spatial resolution of 30 m from the Shuttle Radar Topography Mission (SRTM).

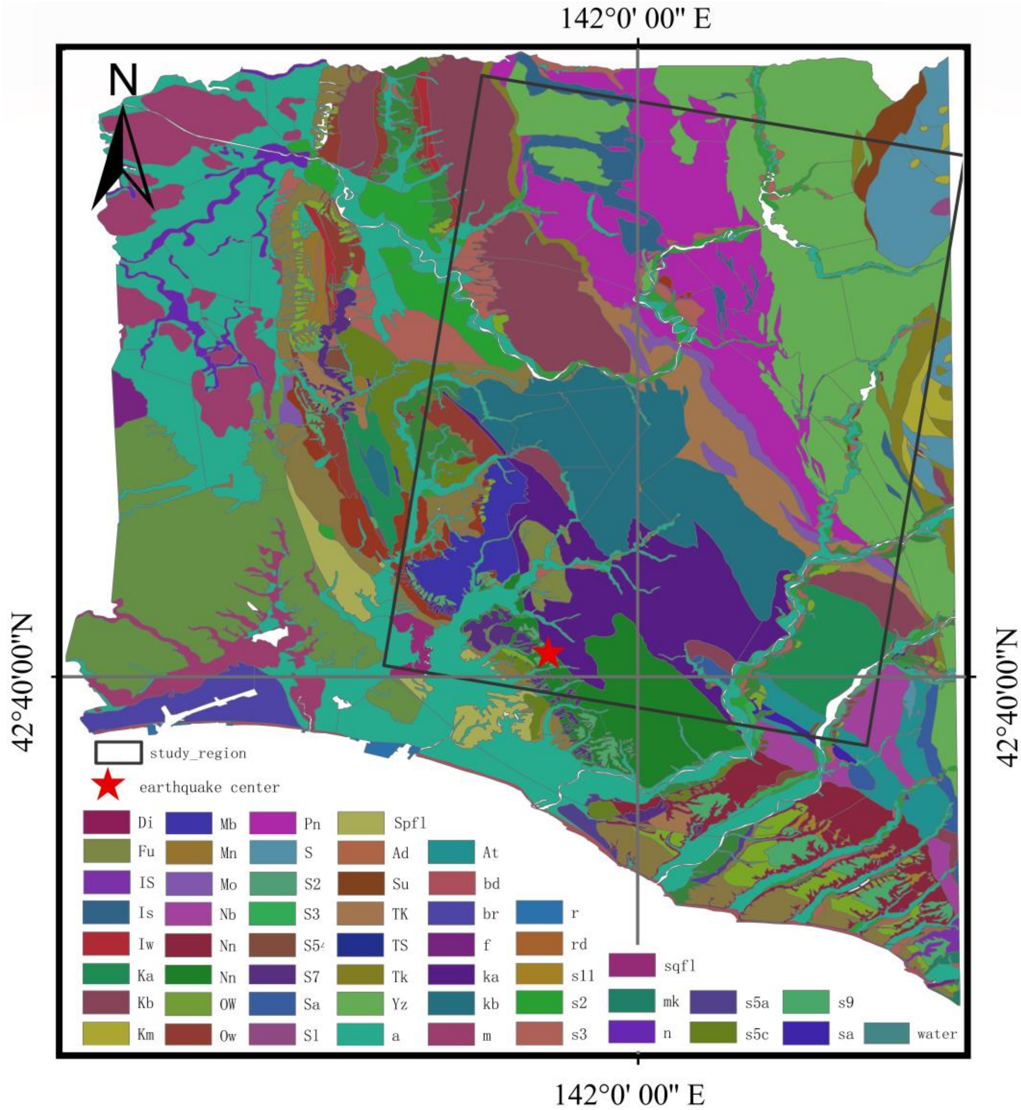

Figure 2. Geological map resvised by authors form Ozkai and Komatsubara [25].

Table 1. Basic parameters of SAR datasets.

Data	Orbit	Polarization	Incidence	Spatial Resolution (Range × Azimuth)	Time Interval
(yyyy/mm/dd)			Angle (°)	(m)	(Days)
2017/06/15	D18	HH	36.2	3 × 1	−400
2017/11/16	D18	HH	36.2	3 × 1	−300
2018/05/03	D18	HH	36.2	3 × 1	−113
2018/07/26	D18	HH	36.2	3 × 1	−40
2018/08/23	D18	HH	36.2	3 × 1	−13
2018/09/06 [1]	D18	HH	36.2	3 × 1	0
2018/10/18	D18	HH	36.2	3 × 1	32
2018/11/15	D18	HH	36.2	3 × 1	59
2019/05/02	D18	HH	36.2	3 × 1	246
2019/11/14	D18	HH	36.2	3 × 1	400

[1] The acquisition time of the scene data is 6 September 2018 (11: 40 AM JST), and the earthquake event occurred on 6 September 2018 (3: 08 AM JST).

2.3. InSAR Processing

Berardino et al. [12] were the first to propose the SBAS-InSAR approach. This approach produces a sequence of interferometric pairs using small spatiotemporal baselines as features, and then uses singular value decomposition (SVD) in the deformation calculation to avoid the rank loss problem that might occur in the least squares solution process. Since the SBAS-InSAR algorithm avoids the spatiotemporal decoherence problem and uses fewer data than the PS-InSAR method, it was used in this work to locate slow-moving landslides and examine the impacts of the Iburi earthquake on the motion processes of slow-moving landslides.

To overcome the situation where pre- and post-earthquake SAR data could not obtain effective interferometric information near the epicenter due to the seismic event, SABS-InSAR processed the pre- and post-earthquake five-view data separately to obtain more information about slow-moving landslide sites close to the epicenter.

In this study, we initially conducted joint registration of the SLC data before setting the temporal and spatial baseline thresholds to 400 days and 300 m, respectively, in order to create multiple interferograms. The combination of temporal and spatial baselines constituting the interference pairs is shown in Figure 3. To remove the influence of speckle noise, the range direction and azimuth direction of all SLC data were multi-viewed using a 4×4 pixel window. Then, using a DEM with a resolution of 30 m, simulated terrain phases were generated, and the impacts of the terrain were eliminated using differencing to make differential interferograms. The MCF algorithm was used to unwrap all differential interferograms. Finally, the SBAS-InSAR approach was used to analyze time-series deformation in the LOS direction. Special consideration should be given to the master and slave image acquisition times of the phase unwrapping maps used in the time-series deformation estimation in this case. When the master image was acquired before the earthquake and the slave image was acquired after the earthquake, a serious decoherence phenomenon was found in the 20 km area around the epicenter, so we processed the 5-view pre-earthquake and 5-view post-earthquake data separately to avoid the situation where obtaining the correct time-series deformation near the epicenter was difficult due to incorrect phase unwrapping information. Figure 4 depicts the main experimental flow.

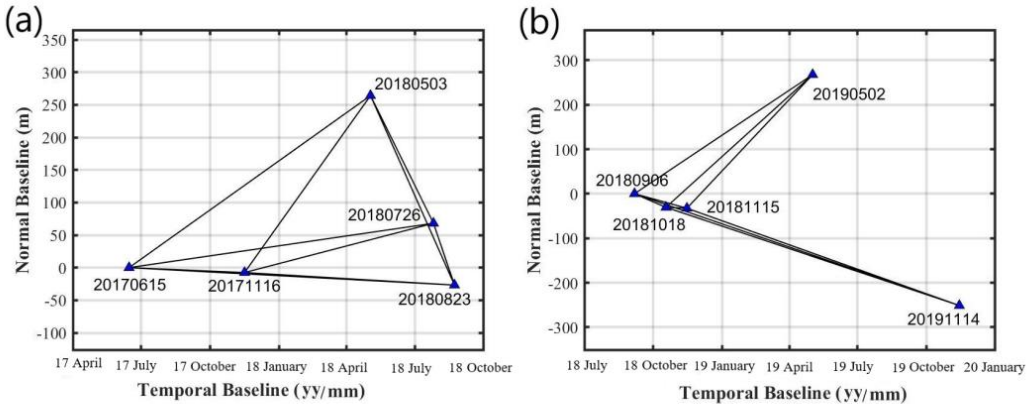

Figure 3. Temporal and spatial baselines of SAR datasets. (**a**) The spatiotemporal baseline combination of pre-earthquake interference pairs. (**b**) The spatiotemporal baseline combination of interference pairs after the earthquake.

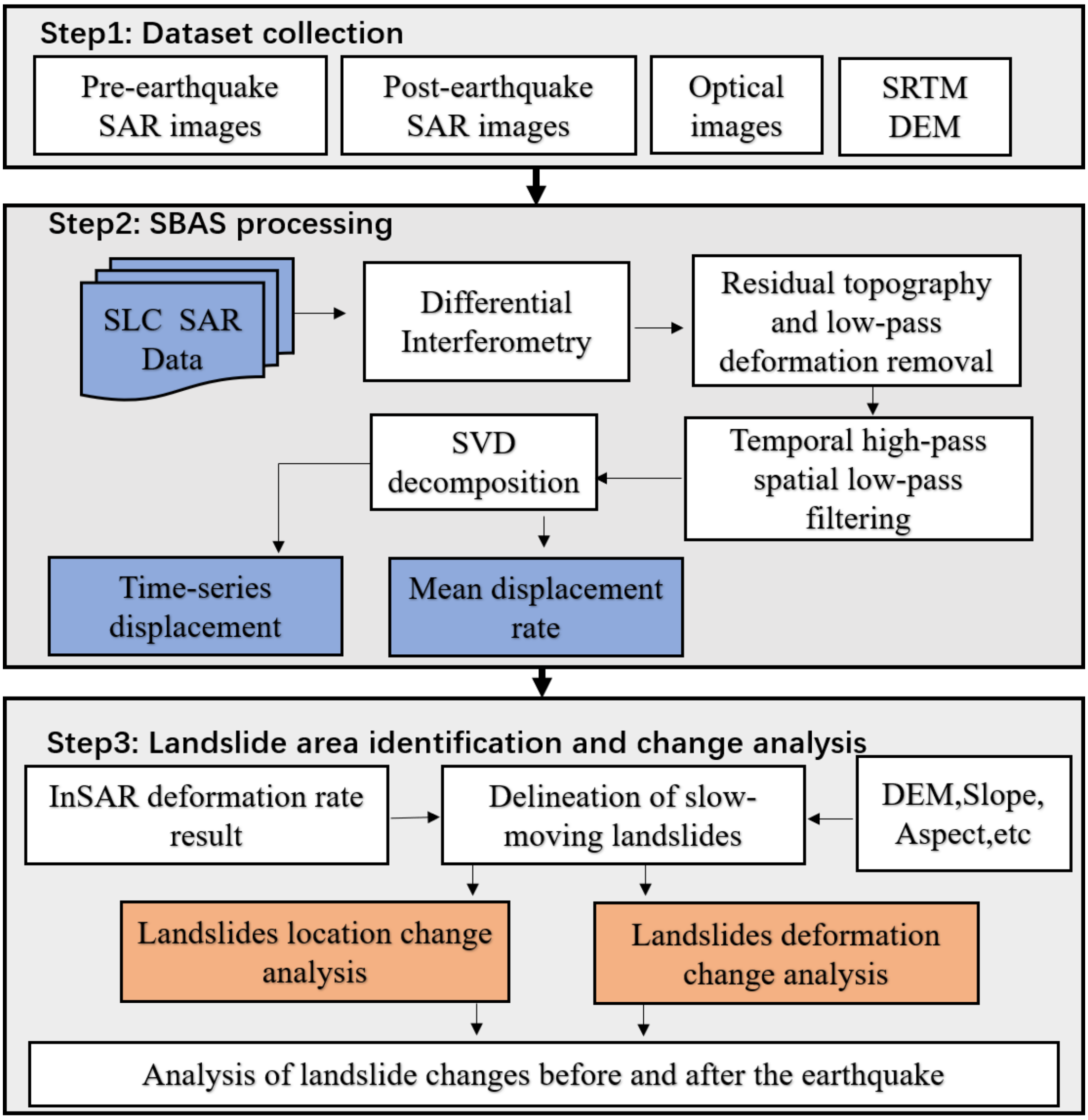

Figure 4. Main flow chart framework in this study.

3. Results

3.1. Identification of Slow-Moving Landslides in Different Periods

Using the SBAS-InSAR algorithm, we tracked the surface deformation of the study region before and after the earthquake. Because InSAR deformation measurements can only detect active regions and cannot be used to determine whether they are slow-moving landslides, we used Google optical images and DEM data to identify slow-moving landslides on slopes with landslide morphological characteristics and significant deformation signals.

Figure 5 shows the distribution of the detected slow-moving landslides after the earthquake. In the range of 33 $\times$ 55 km, 31 slow-moving post-earthquake landslides are distributed in the north of the earthquake center. Except for P23, P8, P5, and P2, the remaining post-earthquake landslides have an area of less than 0.15 km^2, with an elevation between 200 and 500 m a.s.l. In particular, the average annual velocity of landslides (such as P8, P5, P3) far away from the earthquake center is 80 mm/year, while the average annual velocity of landslides (such as P23, P30, P20) near the earthquake center is between 40 and 70 mm/year. In other words, several landslides far away from the earthquake center move faster than those near the earthquake center.

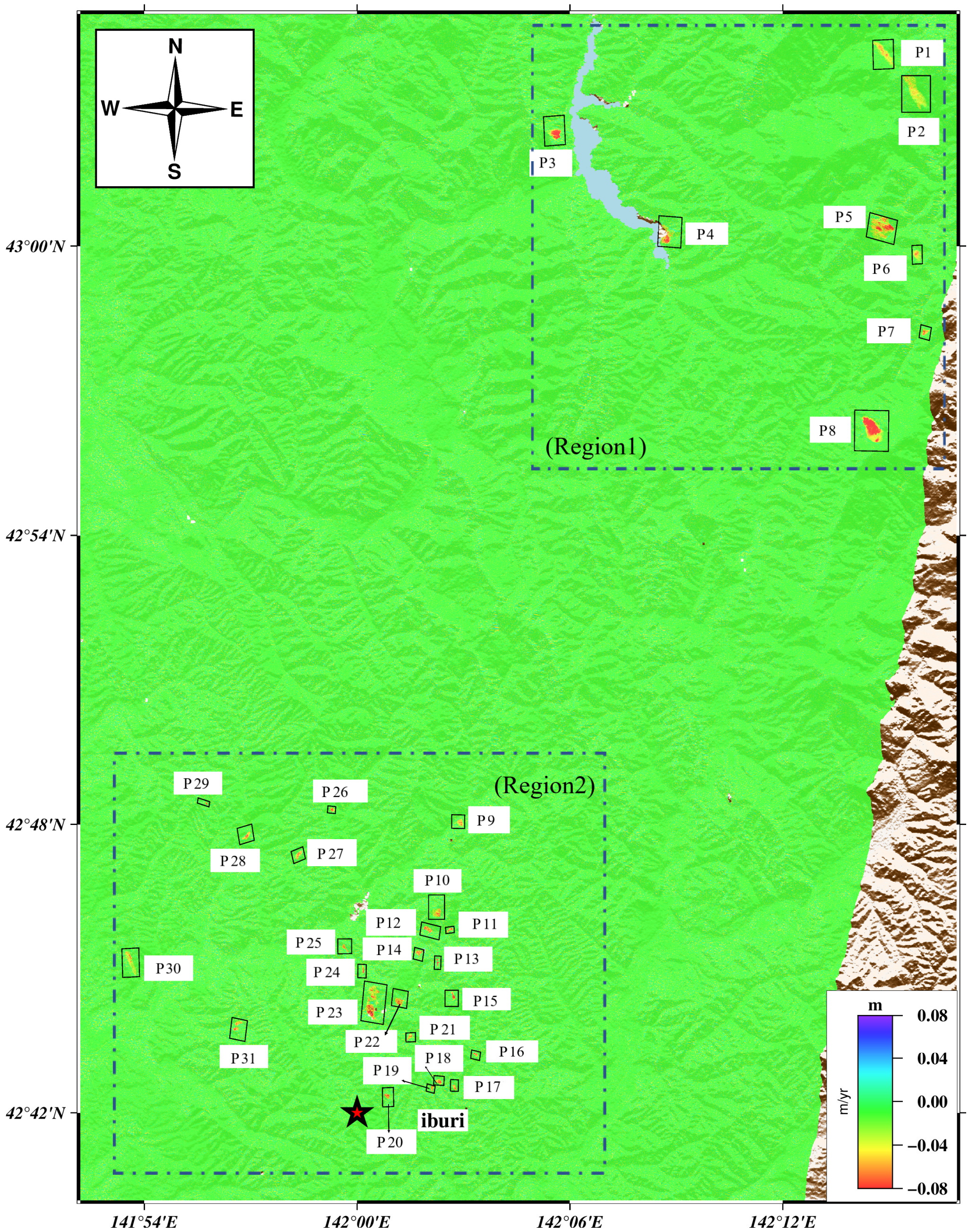

Figure 5. Distribution map of the monitored slow-moving landslides in the post-earthquake period. The average post-earthquake deformation velocity in the Iburi area is derived from the ALOS-2 PALSAR-2 data, and the black boxes indicate the locations of the slow-moving landslides. P1–P30 represent the slow-moving landslides detected in the post-earthquake period. Two typical regions of slow-moving landslides following the earthquake are shown by the blue box lines.

It can be seen from Figure 5 that the slow-moving landslides that were found after the earthquake are densely concentrated in two regions: Region 1, which is located 50 km from the epicenter, and Region 2, which is located 20 km from the epicenter. We discovered 22 slow-moving landslides in Region 2 within a year of the earthquake. The area also saw a significant number of co-seismic landslides as a result of the severe earthquake vibration during the co-seismic period [22]. In Figure 6, 12 typical post-earthquake slow-moving landslides in Region 2 are described, and their positions are contrasted with co-seismic landslides. We discovered that the co-seismic landslides were situated close to slow-moving landslides, and these slow-moving landslides were situated in the upper section of the slope. We can assume that the seismic event significantly affected the stability of the slope in Region 2, even though the locations of the co-seismic landslides and the slow-moving landslides were not entirely consistent. At the same time, we discovered that slow-moving landslides larger than 0.15 km^2, e.g., P23, may have been caused by the long-term activation of sediments from significant co-seismic landslides. Other researchers have also noted these behaviors [17,26]. Other slow-moving landslides, less than 0.1 km^2 in size—such as P14, P20, and P26—were dispersed at the top of the hill.

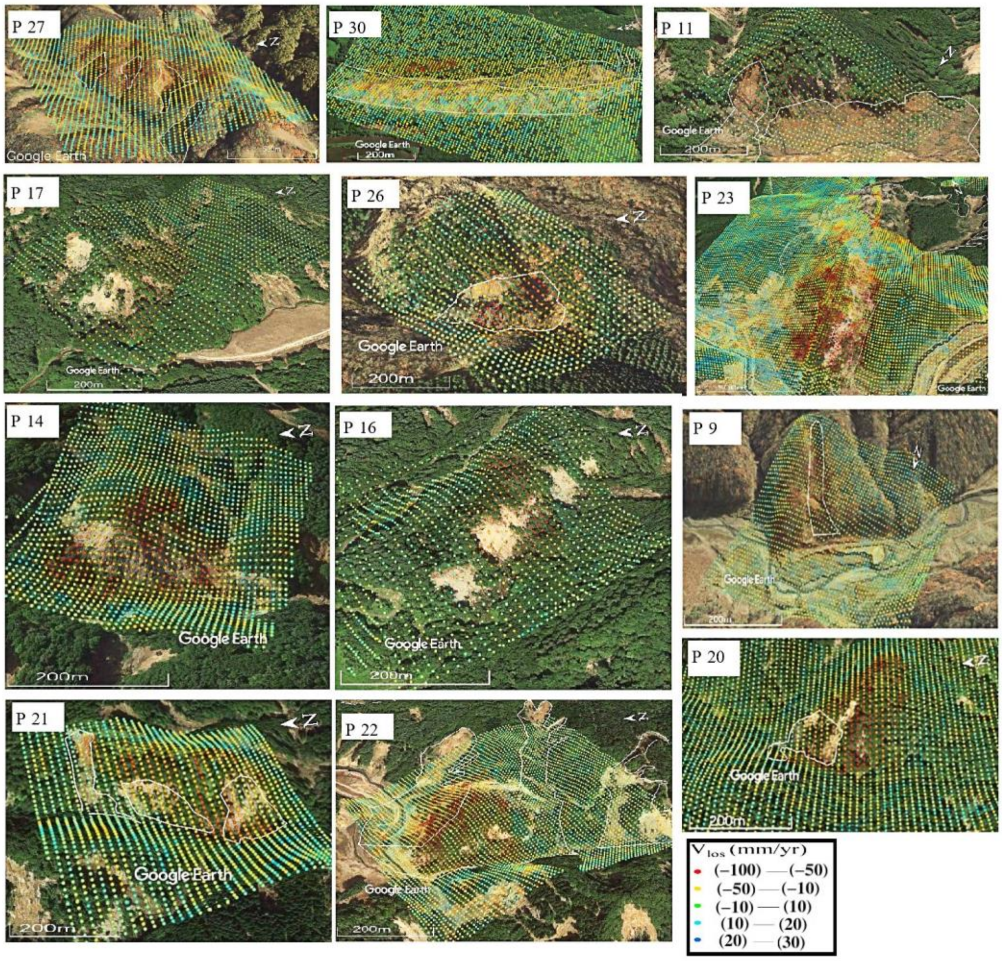

Figure 6. SBAS-InSAR monitoring deformation and optical image interpretation of slow-moving landslides. White lines represent co-seismic earthquake-induced landslide, obtained from Authority of Japan (GSI).

In Figure 7, it is clear that 11 slow-moving landslides existed in the study area prior to the earthquake, but no slow-moving landslides were detected in region 2. It is evident from comparing the distribution of slow-moving landslides before and after the earthquake that the four slow-moving landslides that were present before the earthquake (B11, B8, B7, and B6) are still in motion after the earthquake. The distribution of slow landslides before and after the earthquake was statistically compared from the aspects of the slope, lithology, distance from the epicenter, and topographic position index. The calculation of the slopes used the ArcGIS automatic modeling tool [27]. The topographic position index describes changes in ground elevation, and the closer the number is to zero, the flatter the surface tilt trend [28]. The results are shown in Figure 8. The parameters of the lithology are shown in Table 2. Landslides with signs of activity before the earthquake and no signs of activity after the earthquake, such as B1, B5, B4, B9, B2, B3, and B10, are distributed in the YZ lithology and Pn lithology.

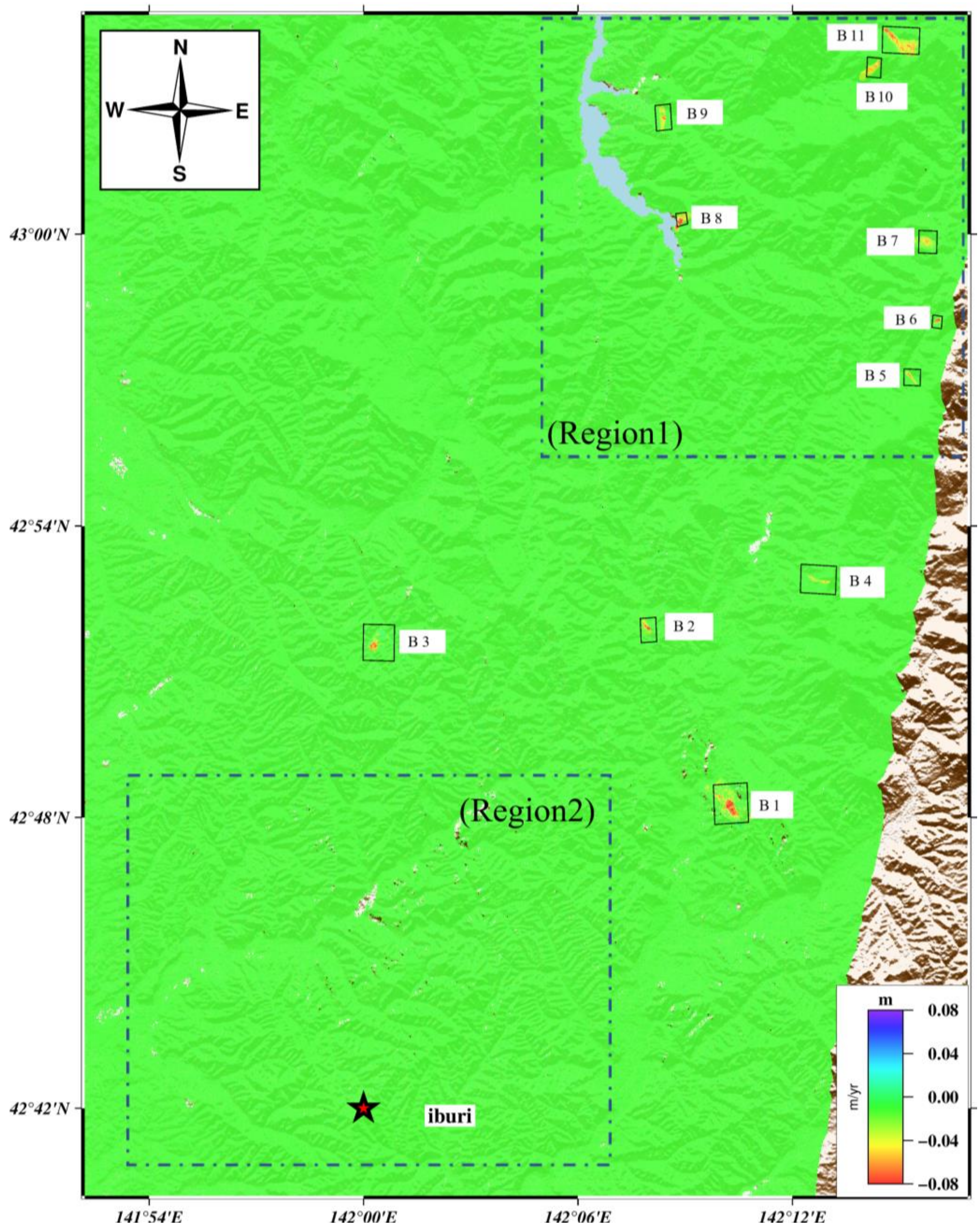

Figure 7. Distribution map of the monitored slow-moving landslides before the earthquake. The average pre-earthquake deformation velocity in the Iburi area is derived from the ALOS-2 PALSAR-2 data, and the black boxes indicate the locations of the slow-moving landslides. B1–B11 represent the slow-moving landslides detected in the pre-earthquake period.

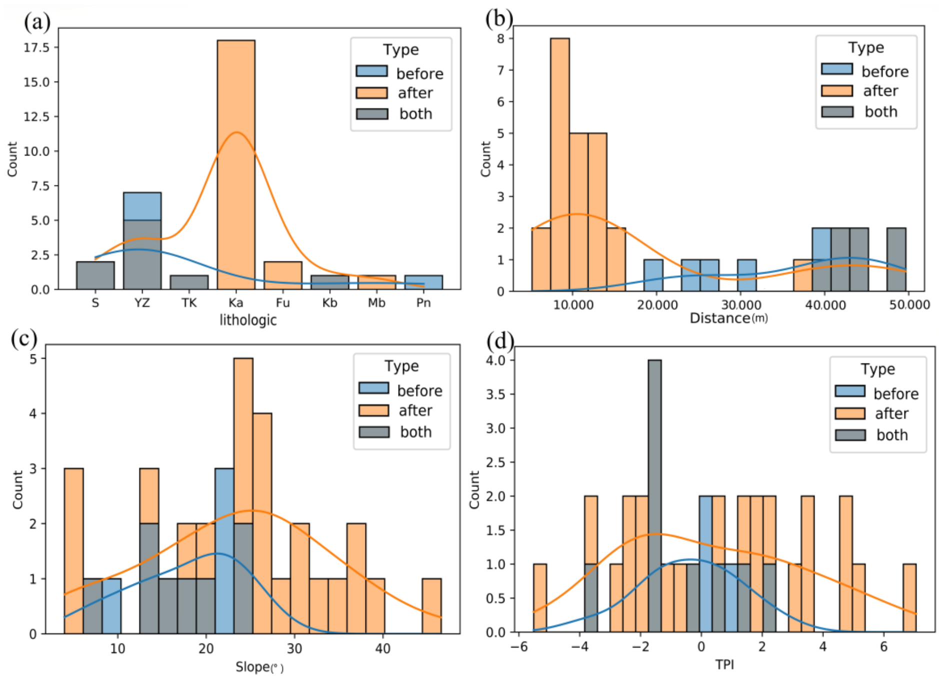

Figure 8. The distribution of slow-moving landslides before and after the earthquake with respect to (**a**) lithology, (**b**) distance from epicenter, (**c**) slope and (**d**) topographic position index.

Table 2. Lithological parameters [1].

Lithology	Lithological Characteristics
Kb	Alternating beds of sandstone and mudstone conglomerate and sandstone
Fu	Alternating beds of sandstone and mudstone conglomerate and hyaloclastite
YZ	Mudstone, sandstone, and conglomerate with tuff and limestone
Pn	Siltstone with sandstone and tuff
S	Intrusive rocks
Ka	Diatomaceous to siliceous mudstone and glauconite sandstone with tuff
Mb	Diatomaceous to siltstone with sandstone and conglomerate
TK	Mudstone, sandstone, and alternating beds of sandstone and mudstone, with conglomerate and tuff
Sa	Andesite to dacite lava and Pyroclastic rocks
a	Silt, clay, sand, gravel, and peat
s2	Gravel, sand, and mud, with peat and volcanic ash
s11	Gravel, sand, and mud

[1] The information was provided by the Geospatial Information Authority of Japan (GIAJ).

3.2. Characteristics of Slow-Moving Landslides' Movement in Different Periods

It is clear from the previous subsection that seismic occurrences can cause a lot of slope instabilities, which then develop into slow-moving landslides. However, various landslides respond to earthquake occurrences in different ways. The time series deformations of 37 slow-moving landslides were inverted using the SBAS-InSAR algorithm in order to better understand how the landslides react to the seismic stress perturbation from the time dimension. The reasons for analyzing time series deformations were twofold: First, we can study the movement characteristics of slow landslides by analyzing the time series changes of the landslides. Secondly, determining the movement changes of the landslide before and after the earthquake is helpful for studying the different change patterns of landslides under the action of earthquake events. From the perspective of changes in landslide movement, the change patterns of slow-moving landslides can be roughly divided into four types: (1) continuous movement of the co-seismic landslide after the earthquake; (2) reactivation of the stable slope after the earthquake; (3) acceleration of the slow-moving landslide after the earthquake; (4) stabilization of the slow-moving landslide after the earthquake.

3.2.1. Continuous Movement of the Co-Seismic Landslide after the Earthquake

As previously described, the Iburi earthquake triggered about 7059 co-seismic landslides. Most of these landslides were shallow, and some had high mobility [22]. Due to rainfall in the area during the earthquake, some co-seismic landslides may move along gentle gullies for a long time [29]. By monitoring the deformation of the post-earthquake slope, we found a landslide change pattern in which this earthquake triggered rapidly changing co-seismic landslides that continued to move after the earthquake, including P20–P30, P13, and P10. These slow-moving landslides were distributed within 20 km of the earthquake's center, as shown in Figure 5.

P23 was the most representative landslide. This landslide was situated 7.5 km northeast of the earthquake's epicenter. The landslide had a "U" form and measured roughly 1 km long and 0.5 km wide. The landslide was roughly moving in the southwest direction. Figure 9c illustrates how, as a result of the earthquake, the soil and trees on the slope's top slid down the hill and eventually gathered at the slope's base. As noted in Figure 9a,b, the slope in this area essentially had slight displacement prior to the earthquake. However, after the earthquake, the yearly average deformation velocity in this area reached 80 mm/year. Figure 9d shows the time series deformations of point A before and after the earthquake. We can see that the movement rate of the landslide increased from 10 mm/year before the earthquake to 60 mm/year after the earthquake, especially between 6 September and 18 October 2019, when its movement process dramatically quickened, reaching 0.55 mm/day. Therefore, the co-seismic landslide activated by the Iburi earthquake still continued to move after the earthquake representing a changed pattern of landslide movement in the earthquake area. Such landslides were greatly affected by the earthquake. At least one year after the earthquake, such landslides were still in an unstable state.

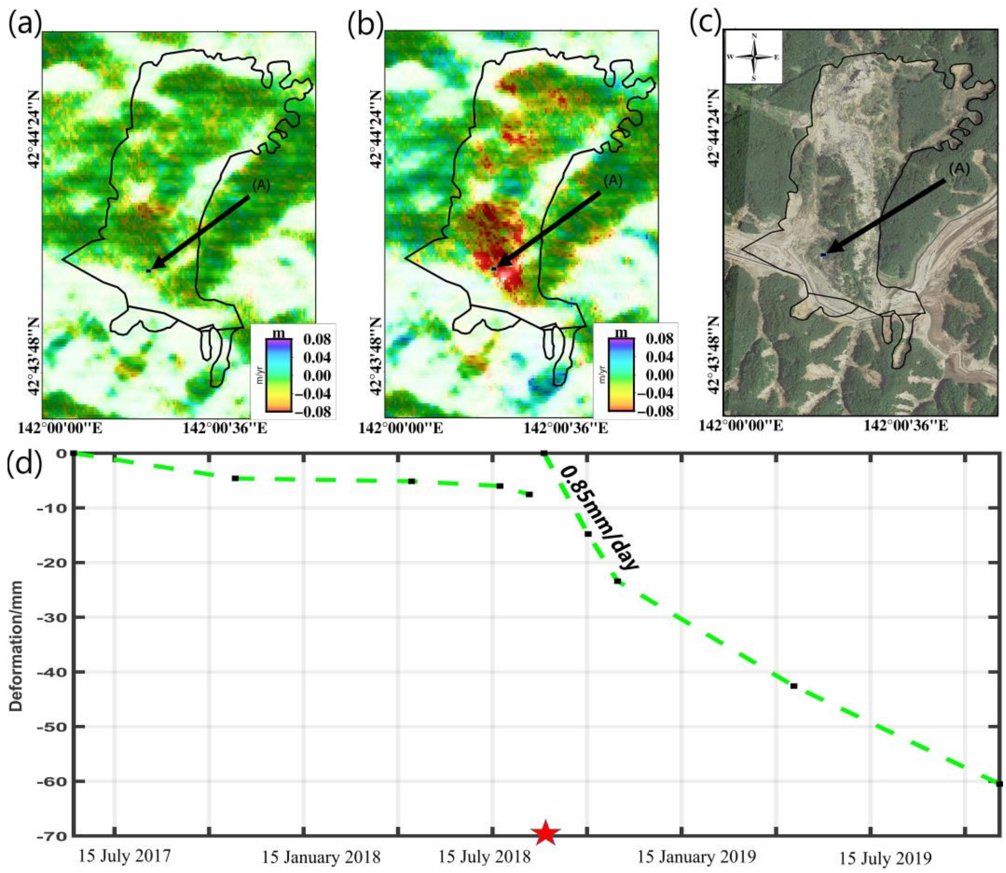

Figure 9. (**a**,**b**) Average LOS deformation velocities of landslide P23 before and after the earthquake, respectively. (**c**) Optical image of landslide P23 during the co-seismic period. (**d**) Time series deformation of point A before and after the earthquake. The pentagram indicates the time of the earthquake.

3.2.2. Reactivation of the Stable Slope after the Earthquake

The earthquake not only continued the co-seismic landslides' movement but also reactivated the stable slope, e.g., P3, P5, P8, and P3. According to Figure 5, these slow-moving landslides were dispersed 35 km to 55 km from the earthquake's epicenter. Before the earthquake, these slow-moving landslides were relatively stable, with little noticeable displacement. There was no rapid sliding during the co-seismic period. However, after the earthquake, these slopes were affected by seismic waves and began to move. P8 is the landslide that most exemplifies this. This slow-moving landslide was located 37 km northeast of the earthquake center, approximately 1.3 km long and 0.8 km wide, and moved downward along the southwest direction of the slide surface. The average annual movement rate of the landslide before and after the earthquake is shown in Figure 10a,b, and the optical image of the landslide is shown in Figure 10c. The time series displacement of point B in the landslide before and after the earthquake is depicted in Figure 9d. The slope did not move more than 5 mm between 15 June and 23 August 2017. However, after the earthquake occurred, the landslide began to accelerate. From 6 September to 18 October 2018, the average daily displacement of the landslide reached 0.6 mm/day. Until November of the second year, this landslide was still moving, totaling 80 mm. Unlike P23, the landslide did not become a co-seismic landslide during the co-seismic phase. Therefore, the reactivation of the stable slope was another type of slow landslide movement in the seismic area.

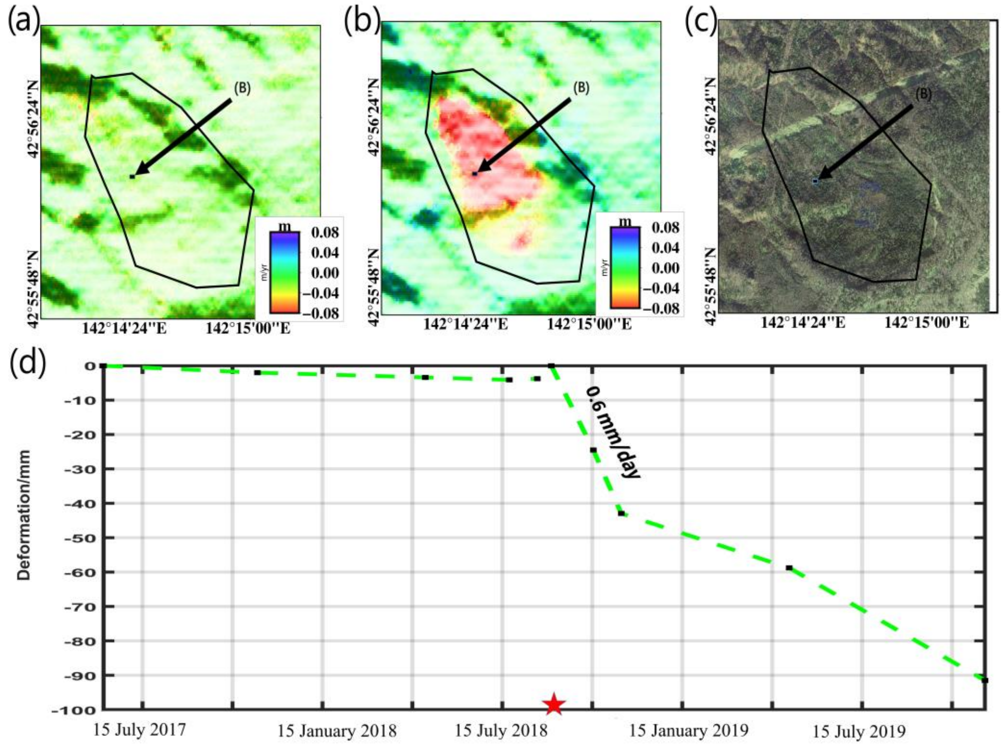

Figure 10. (**a**,**b**) Average LOS deformation velocities of landslide P8 before and after the earthquake, respectively. (**c**) Optical image of landslide P8. (**d**) Time series deformation of point B before and after the earthquake. The pentagram indicates the time of the earthquake.

3.2.3. Acceleration of the Slow-Moving Landslide after the Earthquake

As mentioned above, landslides in different environmental conditions have different response patterns to seismic events. In addition to the two types of landslides mentioned above, another kind of landslide was those that were already moving slowly before the earthquake and accelerated after the earthquake, such as P1, P4, P6, and P7. These landslides were dispersed between 40 and 50 km from the epicenter, as shown in Figure 5. These landslides had been moving slowly before the earthquake and continued to move after the earthquake, although within two months following the earthquake, they began to accelerate. Landslide P1, which was 50 km northeast of the epicenter, is a typical example of this type of landslide. The landslide was 0.2 km broad and 1.0 km long. The average displacement of this landslide before and after the earthquake is depicted in Figure 11a,b. The slow-moving landslide's ground cover is depicted in Figure 11c, and the displacement variations of the slow landslide's center (point C) are shown in Figure 10d. The slope moved by more than 50 mm between 15 June and 23 August 2019, as can be seen. Since the earthquake on 6 September 2018, the landslide has been moving, and compared to the time before the accident, its rate of movement accelerated in the month that followed. Within 70 days after the earthquake, the daily displacement was close to 0.5 mm/day, and the total displacement one year after the earthquake also reached 50 mm. The details of the time series deformation show that this type of landslide was affected by the seismic event and exhibited accelerated movements in the two months after the earthquake. Thus, the earthquake would have accelerated the slow-moving landslide and changed its movement pattern.

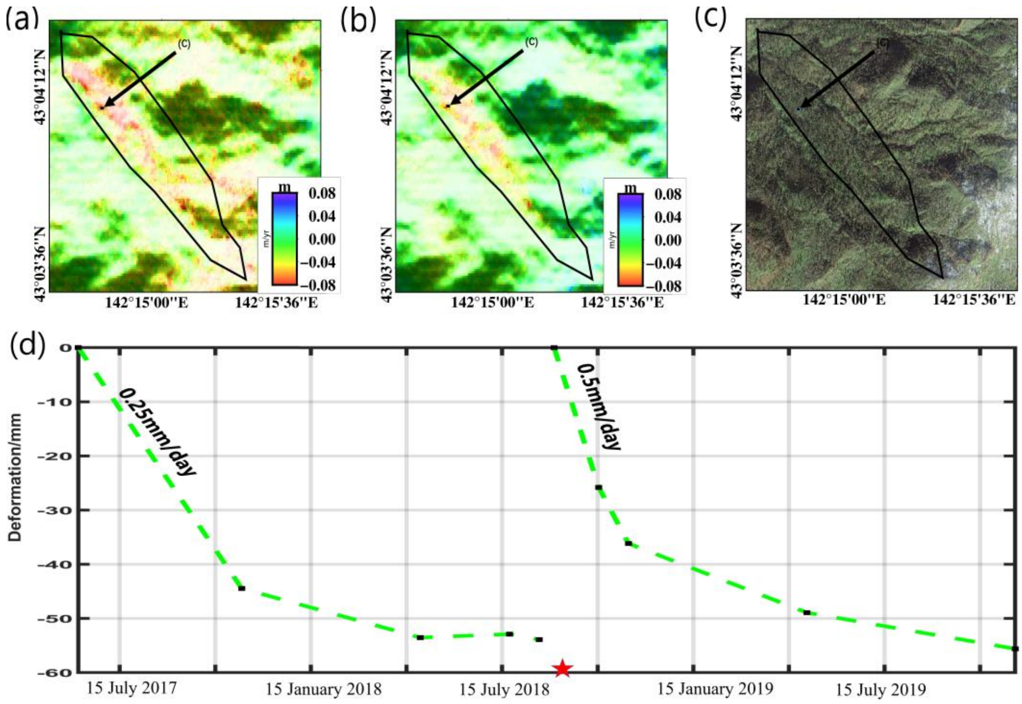

Figure 11. (**a**,**b**) Average LOS deformation velocities of landslide P1 before and after the earthquake, respectively. (**c**) Optical image of landslide P1. (**d**) Time series deformation of point C before and after the earthquake. The pentagram indicates the time of the earthquake.

3.2.4. Stabilization of the Slow-Moving Landslide after the Earthquake

In addition to the above three kinds of landslides, this kind of landslide was in a state of slow motion before the earthquake, but the landslide was stable after the earthquake, and there was no obvious displacement after the earthquake, e.g., B1, B5, B4, B9, B2, B3, and B10. Figure 7 depicts the locations of these landslides, which were between 25 and 50 km from the epicenter. Take landslide B1 as an example; the landslide was 27 km northeast of the earthquake's center and was approximately 0.7 km long and 0.5 km wide. The average displacement of this landslide within a year before and after the earthquake is depicted in Figure 12a and b, respectively. Figure 12d shows the time-series displacement changes of point D of the slow-moving landslide before and after the earthquake. It is noteworthy that the slope remained in a steady state with no discernible displacement after the Iburi earthquake.

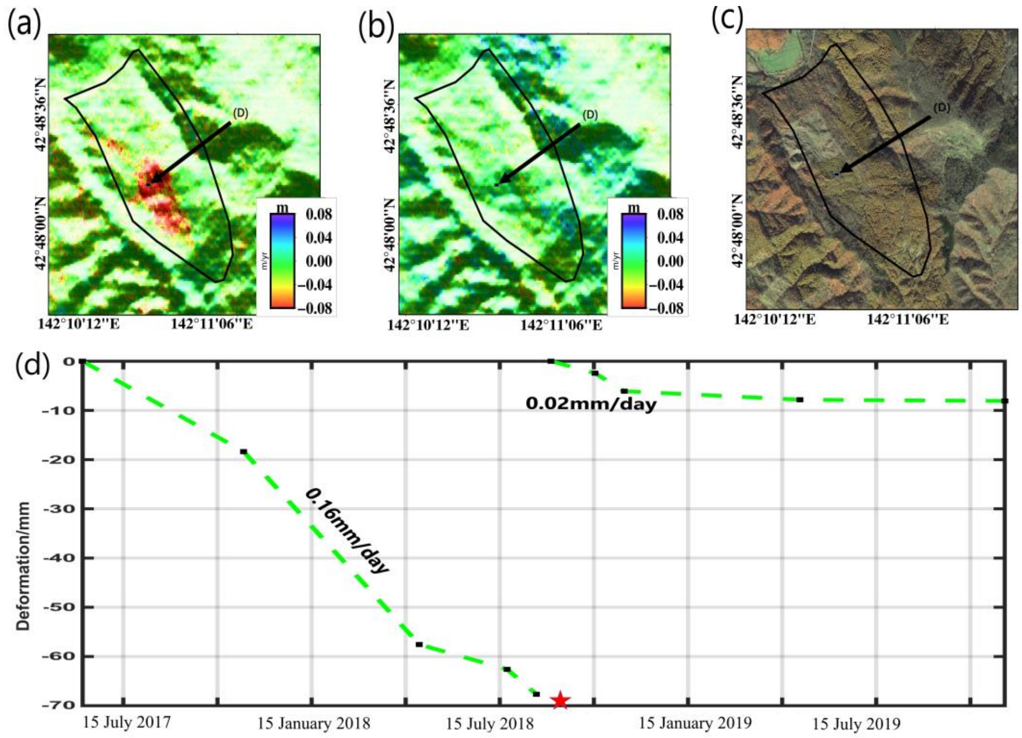

Figure 12. (**a**,**b**) Average LOS deformation velocities of landslide B1 before and after the earthquake, respectively. (**c**) Optical image of landslide B1. (**d**) Time series deformation of point D before and after the earthquake. The pentagram indicates the time of the earthquake.

4. Discussion

4.1. Influence of Earthquake on Slow-Moving Landslides

The 2018 Iburi earthquake resulted in more than 7000 co-seismic landslides, which represent the most obvious example of how earthquakes affect the stability of slopes. However, the impact of the earthquake on the slow-moving landslides in this region is yet unknown. Here, we present a preliminary analysis of the earthquake's impact on slow-moving landslides' stability in both the spatial and temporal dimensions. According to the spatial distribution of slow-moving landslides before and after the earthquake (Figures 5 and 7), there were considerably more slow-moving landslides in the seismic area after the earthquake. Around 85% of the new slow-moving landslides were located within 20 km of the earthquake's epicenter, i.e., Region 2 (Figure 5). Landslides P27, P22, P23, P27, and P11 are typical examples of new slow-moving landslides in this area that were situated close to co-seismic landslides (Figure 8). Other landslides, such as P17, P14, and P9, were situated at the top of sloping terrain and located in the near-field area of the earthquake (Figure 6). These events show that some co-seismic landslides continue ongoing displacement within a year of the earthquake, as did their sediments or loose deposits, e.g., P23 (Figure 9). However, some slopes close to the earthquake's epicenter were continuously subjected to the influence of strong seismic vibration; although these did not result in co-seismic landslides, their stability was damaged [16,25]. Although the energy generated by the earthquake was insufficient to cause co-seismic landslides in the proximity of 50 km away from the epicenter, it was sufficient to accelerate the activity of slow-moving landslides and to activate the movement of dormant landslides in this region (Figures 10 and 11). Here, we collected the Modified Mercalli Intensity (MMI) data from ShakeMap (https://earthquake.usgs.gov/data/shakemap/, accessed on 2 March 2023). From Figure 13, we can see that 85% of slow-moving landslides after the earthquake were distributed between the seismic intensity VI–VIII, which also shows that there was a strong relationship between the occurrence of slow-moving landslides after the earthquake and the earthquake from the spatial distribution.

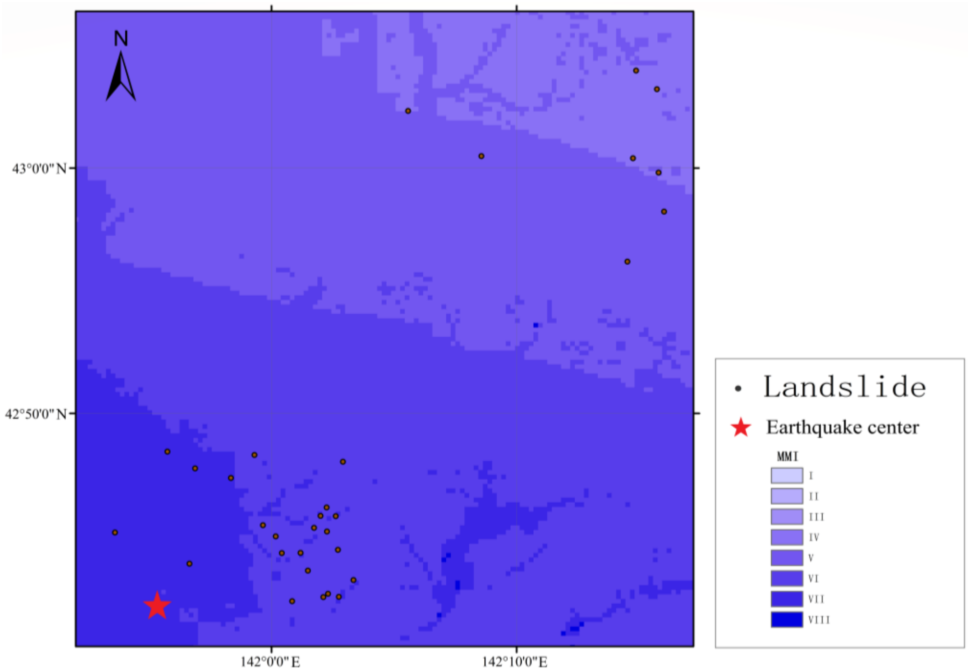

Figure 13. Modified Mercalli Intensity (MMI) and the distribution of slow-moving landslides after the earthquake.

Here, we need to clarify the following: The LOS value obtained by InSAR is obtained by projecting the deformation of the real three-dimensional surface to the LOS direction. The positive value of the LOS deformation rate represents that the observation object is close to the satellite, and the negative value of the LOS deformation rate represents that the observation object is far away from the satellite. Moreover, the LOS direction is sensitive to the difference of deformation in different directions of the surface and is most sensitive to the vertical direction, followed by the east–west direction and finally the north–south direction [30]. Here, we are more concerned about the movement of the landslide than the direction of the landslide. Of course, the direction of landslide movement may have an impact on the LOS value. For example, when the landslide's slope is near the east, the horizontal component of the downward-moving slope body similarly increases the LOS value when the slope value is greater than 36.2 degrees, e.g., P5, P2, P20, P18, and P25. When the direction slope is close to the west and the slope value is less than 53.8 degrees, the horizontal component of downward-moving slope bodies also increases the value of LOS direction, e.g., P23, P15, P11, P16, and P31.

We divided the deformation into three levels to compare the changes of unstable areas before and after the earthquake, namely, the heavy subsidence area (<−6 mm/month), the slight subsidence area −6~−0.5 mm/month), and the stable area (−0.5~0.5 mm/month), as shown in Table 3. After the earthquake, the area of serious subsidence increased significantly, from 1.67 km^2 to 2.56 km^2. Therefore, the effect of earthquakes on slow-moving landslides is also notable from the perspective of the movements in the temporal dimension.

Table 3. Comparison of subsidence area changes in different periods.

Data	Severe Subsidence	Light Subsidence	Stable Area
(dd mm yyyy)	(km^2)	(km^2)	(km^2)
15 June 2017	0	0	0
16 November 2017	1.29	3.21	1920.50
3 May 2017	1.28	2.98	1920.74
26 July 2018	1.42	2.87	1920.71
23 August 2018	1.67	3.51	1919.83

Table 3. *Cont.*

Data (dd mm yyyy)	Severe Subsidence (km^2)	Light Subsidence (km^2)	Stable Area (km^2)
6 September 2018 [1]	0	0	0
18 October 2018	2.56	5.06	1917.38
15 November 2018	2.42	4.74	1917.84
2 May 2019	1.92	3.89	1919.19
14 November 2019	1.42	3.45	1920.13

[1] The acquisition time of the scene data is 6 September 2018 (11: 40 AM JST), and the earthquake event occurred on 6 September 2018 (3: 08 AM JST).

4.2. Other Factors That May Affect the Distribution and Variability of Slow-Moving Landslides

Previous studies have shown that there is a strong correlation between co-seismic landslides and epicentral distance, as well as ground motion intensity [31]. The influencing elements, however, are more complex for the occurrence and changing process of slow-moving landslides in seismic zones. The distribution of slow-moving landslides on slopes, distance from the earthquake center, topographic position index, and lithology is not entirely consistent before and after the earthquake (Figure 8). In addition, we compared the relationship between the distribution of slow-moving landslides and rainfall in time and space. First of all, strong rainfall plays an important role in the movement of slow-moving landslides (Figure 14). Before the earthquake, the rainfall reached the extreme value of this period in June 2018, and the area of strong subsidence area also showed an upward trend one month later. Consequently, we assume that one of the factors contributing to the rise in slow-moving landslides following the earthquake may potentially be rainfall. It can be seen from Figure 15 that the precipitation in the week after the earthquake was significantly higher than that in the week before the earthquake, and the spatial distribution of landslides after the earthquake was located in the area of increased precipitation (data from https://disc.gsfc.nasa.gov/datasets?keywords=GPM&page=1, accessed on 2 March 2023). The rise in precipitation in the near-earthquake field region is less than in the far-earthquake field region, and we infer that, contrary to Figure 15, the occurrence of slow-moving landslides in the near-earthquake zone is driven more by seismic impacts than by precipitation.

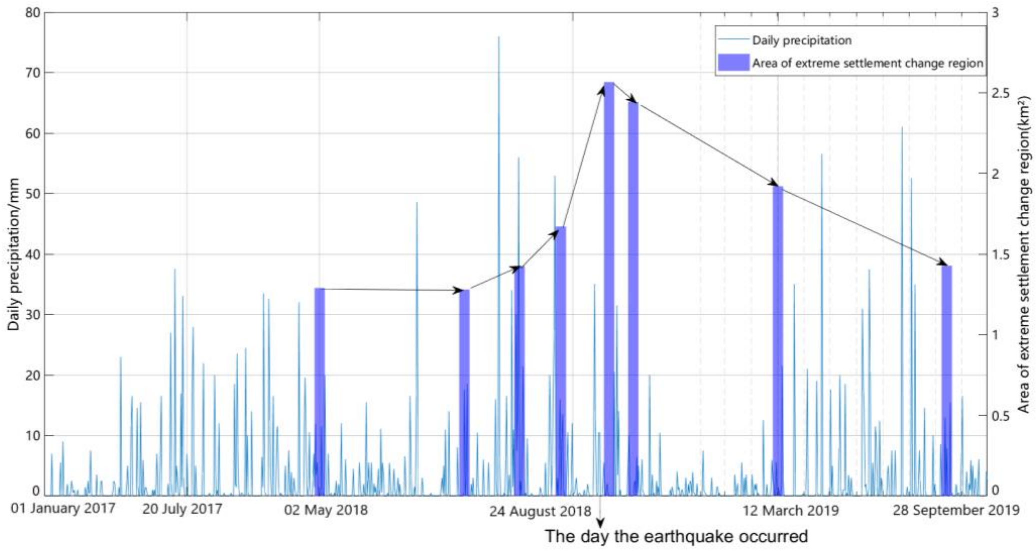

Figure 14. Daily precipitation and strong subsidence area during the study period. Source: Japan Meteorological Agency.

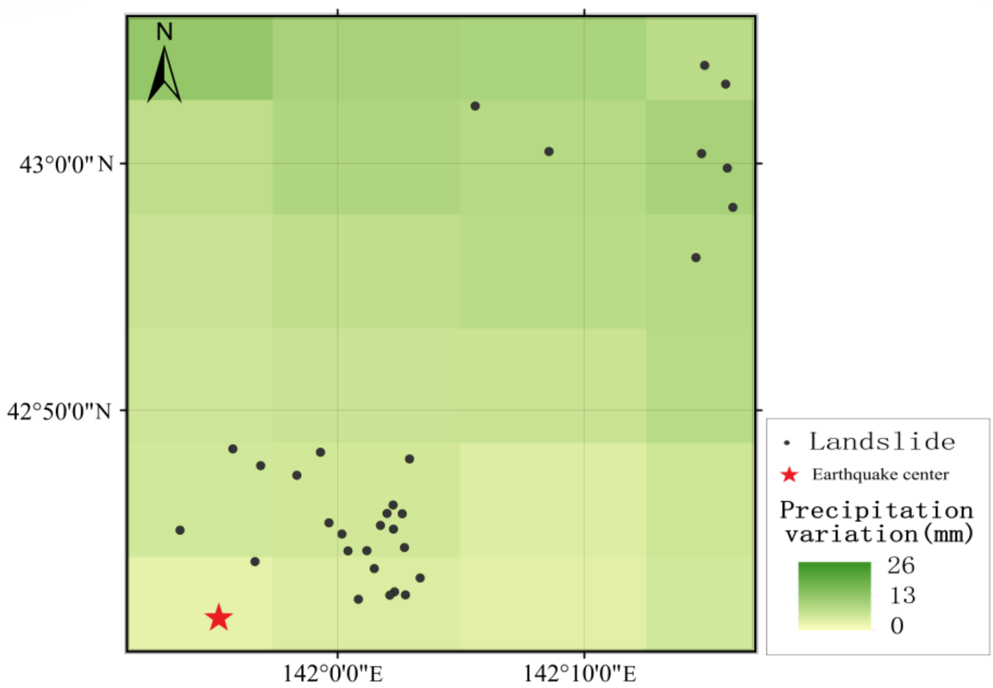

Figure 15. The spatial variation of rainfall before and after the earthquake and the distribution of slow-moving landslides after the earthquake.

In Section 3.2.4, we discovered the interesting phenomenon that some slow-moving landslides before the earthquake were in a stable state after the earthquake, e.g., landslide B1 (Figure 12). The landslide was in motion from 15 June 2017 to 23 August 2018, with a displacement of more than 60 mm. This kind of landslide is distributed in YZ and Pn lithology. The YZ and Pn lithology has higher sandstone content, while the Ka lithology has higher mudstone content [32]. According to studies, sandstone is more permeable than mudstone, and the infiltrated rainwater passes through sandstone as unsaturated gravity flow to reach the base layer [29]. As a result, the slope with YZ and Pn lithologies is more sensitive to soil water content. In contrast, mudstones produce saturated underground storm flows because of their impermeability, so slopes with Ka lithology are more likely to experience landslides due to intense stress. Additionally, Figure 8 shows that this kind of slow-moving landslide is more likely to be dispersed in regions with lower slopes before the earthquake. Meanwhile, as they have robust and permeable lithology, seismic shaking has limited groundwater effects [33]. Similar landslide behaviors were seen in the Nepalese Trishuli River Basin, where six slow-moving landslides with velocities of more than 20 mm/year were not accelerated by the 2015 Mw 7.8 Nepal earthquake [15]. According to the distribution of slow-moving landslides' lithology (Figure 16d), these landslides are most commonly found in regions with diatomaceous to siliceous mudstone, glauconite sandstone, and tuff (Ka). The earthquake undermines the integrity of the soil cover and the existing landslide sediments in this unstable geological and geomorphological environment, causing them to alter at a faster rate under the influence of seismic force [34]. Sandstone hyaloclastite sites with alternating strata of sandstone and mudstone conglomerate sandstone (Kb) are where co-seismic landslides are more widespread than in Figure 16e. After the earthquake, there were a few slow-moving landslides along the Kb area. The majority of the slow-moving landslides, however, occurred in Ka. This shows that lithology is also an important factor affecting the post-earthquake stability of slopes in this area.

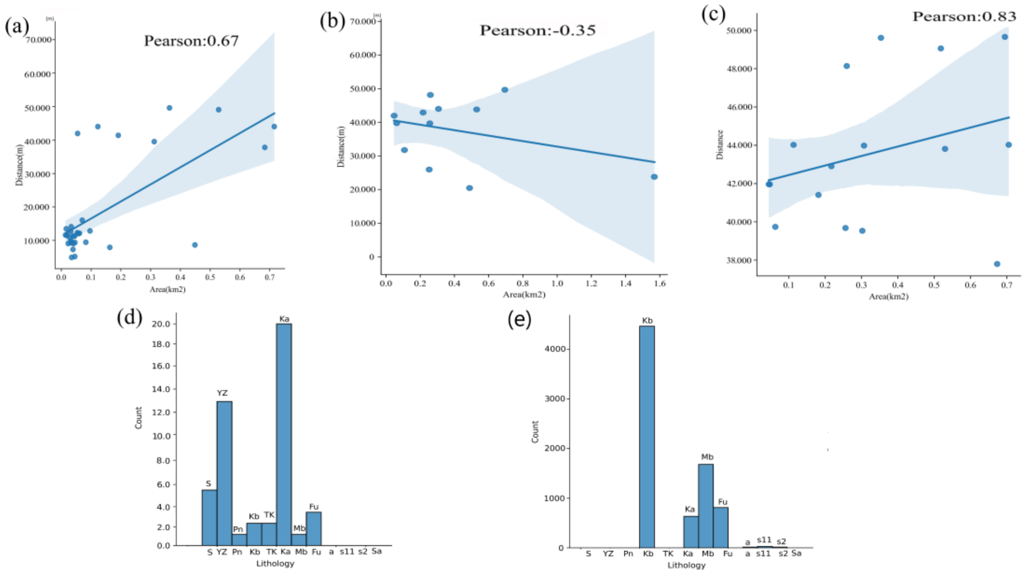

Figure 16. (**a**) The link between the landslide area and the epicentral distance after the earthquake. (**b**) The link between the landslide area and the epicentral distance before the earthquake. (**c**) The link between landslide area and epicenter distance in the far-field region. (**d**) The lithological distribution of slow-moving landslides. (**e**) The lithological distribution of co-seismic landslides, using information from the GSI.

Previous studies have shown that the distribution of slow-moving landslides in the earthquake area has a certain relationship with the area of the landslide itself [17]. Here, we also compare the correlation coefficient between the landslide area and the distance from the epicenter (Figure 16a,b), and the relationship between the landslide area and the epicenter distance in the far-field region (Figure 16c), respectively. There was a negative correlation between the landslide area before the earthquake and the distance from the epicenter. In other words, large-scale landslides were often distributed near the epicenter, while large-scale landslides after the earthquake were usually located far away from the epicenter. Briefly, 90% of the size of slow landslides 20 km away from the epicenter was greater than 0.1 km^2, whereas 95% of the area of slow landslides within 20 km from the epicenter was less than 0.1 km^2. Therefore, the slow-moving landslide size in the far field was usually larger than that in the near field. This indicates that there is a strong relationship between the occurrence of landslides in the far-seismic field and their own size.

5. Conclusions

It has been challenging to comprehend the mechanisms by which seismic occurrences cause landslides, due to a paucity of field data. This research underlines the non-negligible influence of seismic events on landslides in the spatial and temporal dimensions by monitoring deformations of slow-moving landslides before and after the 2018 Iburi earthquake, which were estimated from 10 ALOS-2 PALSAR-2 images based on the SBAS-InSAR algorithm. The findings indicate that the earthquake significantly altered the slow-moving landslides in the seismic area, in addition to resulting in numerous co-seismic landslides. First, following the earthquake, there was a sharp increase in the number of slow-moving landslides, and there was a positive correlation between the intensity distribution of the earthquake event and the slow-moving landslides. Slow-moving landslides were both accelerated and stabilized by the earthquake. Different change patterns showed complex interactions with the region's geological features, as well as with the area of the landslide itself, in addition to having a strong relationship with the seismic event. The study of various changing patterns is crucial for the creation of diverse landslide disaster warning plans.

Author Contributions: Conceptualization, Q.S. and C.H.; methodology, Q.S. and C.H.; software, J.H.; validation, Q.S. and R.G.; formal analysis, C.H., Q.S. and R.G.; resources, Q.S., J.H. and R.G.; writing—original draft preparation, C.H. and Q.S.; writing—review and editing, all authors; supervision, Q.S. and J.H.; funding acquisition, Q.S. and J.H. All authors have read and agreed to the published version of the manuscript.

Funding: This research was funded by the Nature Science Foundation of Hunan Province (grant number 2022JJ30031), the National Natural Science Foundation of China (grant numbers 42030112, 42201432), and the Science and Technology Innovation Program of Hunan Province (grant number 2022RC3042).

Data Availability Statement: The SAR images acquired by ALOS-2 were downloaded from the Japan Aerospace Exploration Agency (JAXA) (https://gportal.jaxa.jp/gpr, accessed on 1 April 2023). The Shuttle Radar Topography Mission (SRTM) DEM, with a resolution of ~30 m/pixel, was downloaded from the National Aeronautics and Space Administration (https://data.nasa.gov, accessed on 1 April 2023).

Acknowledgments: We are very grateful for the ALOS-2 data provided by the Japan Aerospace Exploration Agency (JAXA).

Conflicts of Interest: The authors declare no conflict of interest.

References

1. Keefer, D.K. Landslides Generated by Earthquakes: Immediate and Long-Term Effects. *Treatise Geomorphol.* **2013**, *5*, 250–266. [CrossRef]
2. Chigira, M.; Wu, X.; Inokuchi, T.; Wang, G. Landslides induced by the 2008 Wenchuan earthquake, Sichuan, China. *Geomorphology* **2010**, *118*, 225–238. [CrossRef]
3. Fan, X.; Scaringi, G.; Korup, O.; West, A.J.; van Westen, C.J.; Tanyas, H.; Hovius, N.; Hales, T.C.; Jibson, R.W.; Allstadt, K.E.; et al. Earthquake-Induced Chains of Geologic Hazards: Patterns, Mechanisms, and Impacts. *Rev. Geophys.* **2019**, *57*, 421–503. [CrossRef]
4. Lissak, C.; Bartsch, A.; De Michele, M.; Gomez, C.; Maquaire, O.; Raucoules, D.; Roulland, T. Remote Sensing for Assessing Landslides and Associated Hazards. *Surv. Geophys.* **2020**, *41*, 1391–1435. [CrossRef]
5. Mondini, A.C.; Santangelo, M.; Rocchetti, M.; Rossetto, E.; Manconi, A.; Monserrat, O. Sentinel-1 SAR amplitude imagery for rapid landslide detection. *Remote Sens.* **2019**, *11*, 760. [CrossRef]
6. Yi, Y.; Zhang, W. A new deep-learning-based approach for earthquake-triggered landslide detection from single-temporal RapidEye satellite imagery. *IEEE J. Sel. Top. Appl. Earth Obs. Remote Sens.* **2020**, *13*, 6166–6176. [CrossRef]
7. Li, G.; West, A.J.; Densmore, A.L.; Hammond, D.E.; Jin, Z.; Zhang, F.; Wang, J.; Hilton, R.G. Connectivity of earthquake-triggered landslides with the fluvial network: Implications for landslide sediment transport after the 2008 Wenchuan earthquake. *J. Geophys. Res. Earth Surf.* **2016**, *121*, 703–724. [CrossRef]
8. Karakas, G.; Nefeslioglu, H.A.; Kocaman, S.; Buyukdemircioglu, M.; Yurur, T.; Gokceoglu, C. Derivation of earthquake-induced landslide distribution using aerial photogrammetry: The January 24, 2020, Elazig (Turkey) earthquake. *Landslides* **2021**, *18*, 2193–2209. [CrossRef]
9. Han, Z.; Li, Y.; Du, Y.; Wang, W.-D.; Chen, G. Noncontact detection of earthquake-induced landslides by an enhanced image binarization method incorporating with Monte-Carlo simulation. *Geomat. Nat. Hazards Risk* **2019**, *10*, 219–241. [CrossRef]
10. Jiang, Y.; Liao, M.; Zhou, Z.; Shi, X.; Zhang, L.; Balz, T. Landslide Deformation Analysis by Coupling Deformation Time Series from SAR Data with Hydrological Factors through Data Assimilation. *Remote Sens.* **2016**, *8*, 179.
11. Hooper, A.; Zebker, H.; Segall, P.; Kampes, B. A new method for measuring deformation on Volcanoes and other natural terrains using InSAR Persistent Scatterers. *Geophyiscal Res. Lett.* **2004**, *31*, 1–5. [CrossRef]
12. Berardino, P.; Fornaro, G.; Lanari, R.; Sansosti, E. A new algorithm for surface deformation monitoring based on small baseline differential SAR interferograms. *IEEE Trans. Geosci. Remote Sens.* **2002**, *40*, 2375–2383. [CrossRef]
13. Ferretti, A.; Fumagalli, A.; Novali, F.; Prati, C.; Rocca, F.; Rucci, A. A New Algorithm for Processing Interferometric Data-Stacks: SqueeSAR. *IEEE Trans. Geosci. Remote Sens.* **2011**, *49*, 3460–3470. [CrossRef]
14. Wang, X.; Mao, H. Spatio-temporal evolution of post-seismic landslides and debris flows: 2017 Ms 7.0 Jiuzhaigou earthquake. *Environ. Sci. Pollut. Res.* **2022**, *29*, 15681–15702. [CrossRef] [PubMed]
15. Bekaert, D.P.; Handwerger, A.L.; Agram, P.; Kirschbaum, D.B. InSAR-based detection method for mapping and monitoring slow-moving landslides in remote regions with steep and mountainous terrain: An application to Nepal. *Remote Sens. Environ.* **2020**, *249*, 111983. [CrossRef]
16. Polcari, M.; Montuori, A.; Bignami, C.; Moro, M.; Stramondo, S.; Tolomei, C. Using multi-band InSAR data for detecting local deformation phenomena induced by the 2016–2017 Central Italy seismic sequence. *Remote Sens. Environ.* **2017**, *201*, 234–242. [CrossRef]
17. Song, C.; Yu, C.; Li, Z.; Utili, S.; Frattini, P.; Crosta, G.; Peng, J. Triggering and recovery of earthquake accelerated landslides in Central Italy revealed by satellite radar observations. *Nat. Commun.* **2022**, *13*, 7278. [CrossRef]

18. Cai, J.; Zhang, L.; Dong, J.; Dong, X.; Li, M.; Xu, Q.; Liao, M. Detection and characterization of slow-moving landslides in the 2017 Jiuzhaigou earthquake area by combining satellite SAR observations and airborne Lidar DSM. *Eng. Geol.* **2022**, *305*, 106730. [CrossRef]
19. Kimura, G. Oblique subduction and collision: Forearc tectonics of the Kuril Arc. *Geology* **1986**, *14*, 404. [CrossRef]
20. Zhao, B.; Wang, Y.; Feng, Q.; Guo, F.; Zhao, X.; Ji, F.; Liu, J.; Ming, W. Preliminary analysis of some characteristics of coseismic landslides induced by the Hokkaido Iburi-Tobu earthquake (5 September 2018), Japan. *Catena* **2020**, *189*, 104502. [CrossRef]
21. Li, R.; Wang, F.; Zhang, S. Controlling role of Ta-d pumice on the coseismic landslides triggered by 2018 Hokkaido Eastern Iburi Earthquake. *Landslides* **2020**, *17*, 1233–1250. [CrossRef]
22. Osanai, N.; Yamada, T.; Hayashi, S.-i.; Kastura, S.y.; Furuichi, T.; Yanai, S.; Murakami, Y.; Miyazaki, T.; Tanioka, Y.; Takiguchi, S. Characteristics of landslides caused by the 2018 Hokkaido Eastern Iburi Earthquake. *Landslides* **2019**, *16*, 1517–1528. [CrossRef]
23. Oglesby, D.D.; Archuleta, R.J.; Nielsen, S.B. Earthquakes on Dipping Faults: The Effects of Broken Symmetry. *Science* **1998**, *280*, 1055–1059. [CrossRef] [PubMed]
24. Ohtani, M.; Imanishi, K. Seismic potential around the 2018 Hokkaido Eastern Iburi earthquake assessed considering the viscoelastic relaxation. *Earth Planets Space* **2019**, *71*, 57. [CrossRef]
25. Ozaki, M.; Komatsubara, T. 1:200,000 Land Geological Map in the Ishikari Depression and Its Surrounding Area with Explanatory Note. 2014. Available online: https://www.gsj.jp/data/coastalgeology/GSJ_SGMCZ_S4_2014_03_b.pdf (accessed on 28 February 2023).
26. Handwerger, A.; Booth, A.; Huang, M.-H.; Fielding, E. Inferring the Subsurface Geometry and Strength of Slow-moving Landslides using 3D Velocity Measurements from the NASA/JPL UAVSAR. *J. Geophys. Res. Earth Surf.* **2021**, *126*, 5898. [CrossRef]
27. Jiménez, J.; Irigaray, C.; Hamdouni, R.; Fernández, P.; Chacón, J. Building models for automatic landslide susceptibility analysis and mapping in ArcGIS. *Geophys. Res. Abstr.* **2007**, *9*, 2.
28. Weiss, A.D. Topographic position and landforms analysis. In Proceedings of the ESRI User Conference, San Diego, CA, USA, 9–13 July 2001; p. 200.
29. Yamagishi, H.; Yamazaki, F. Landslides by the 2018 Hokkaido Iburi-Tobu Earthquake on September 6. *Landslides* **2018**, *15*, 2521–2524. [CrossRef]
30. Hu, J.; Liu, J.; Li, Z.; Wu, L.; Sun, Q.; Wu, W. Estimating three-dimensional coseismic deformations with the SM-VCE method based on heterogeneous SAR observations: Selection of homogeneous points and analysis of observation combinations. *Remote Sens. Environ.* **2021**, *255*, 112298. [CrossRef]
31. Chang, M.; Zhou, Y.; Zhou, C.; Hales, T.C. Coseismic landslides induced by the 2018 Mw 6.6 Iburi, Japan, Earthquake: Spatial distribution, key factors weight, and susceptibility regionalization. *Landslides* **2021**, *18*, 755–772. [CrossRef]
32. Hack, H.; Alkema, D.; Kruse, G.; Leenders, N. Influence of earthquakes on the stability of slopes. *Eng. Geol.* **2007**, *91*, 4–15. [CrossRef]
33. Zhou, H.; Che, A.; Wang, L.; Wang, L. Investigation and mechanism analysis of disasters under Hokkaido Eastern Iburi earthquake. *Geomat. Nat. Hazards Risk* **2021**, *12*, 1–28. [CrossRef]
34. Valagussa, A.; Marc, O.; Frattini, P.; Crosta, G.B. Seismic and geological controls on earthquake-induced landslide size. *Earth Planet. Sci. Lett.* **2019**, *506*, 268–281. [CrossRef]